PNAS RESEARCH ARTICLE | EARTH, ATMOSPHERIC, AND PLANETARY SCIENCES

Water-rich incipient melt of the deep upper mantle indicates locally preserved low-velocity zones above the 410 km discontinuity

Longjian Xie[a,b,c,1], Tomoo Katsura[b], Nobuyoshi Miyajima[b], Tongzhang Qu[c], and Ho-Kwang Mao[a,d,1]

Affiliations are included on p. 7.

Contributed by Ho-kwang Mao; received January 1, 2025; accepted May 5, 2025; reviewed by Nathalie Bolfan-Casanova, Davide Novella, and Xiaozhi Yang

Seismic low-velocity layers (LVLs), frequently attributed to hydrous-silicate melts, are detected globally but exhibit lateral discontinuities. Geophysical and laboratory studies of water content in the mantle transition zone (MTZ) and upper mantle solubility limits suggest these layers likely form through global dehydration melting near the 410 km discontinuity (D410). A key hypothesis posits that melts form globally but are preserved only where melt stability permits retention. However, challenges in quenching melts into glass or fine-grained crystals at mantle pressures have precluded precise determination of melt composition, fueling debates over the mechanisms governing LVLs' sporadic distribution. Here, we developed a fast-quenching high-pressure cell assembly to synthesize hydrous glasses or fine-grained quench crystals at pressures >10 GPa, enabling high-precision analysis of incipient melt composition. Experiments at 13 GPa reveal that the 410 melt contains 43 mol% H_2O, 9.2 mol% CaO, 30.5 mol% (Mg, Fe)O, 0.2 mol% Al_2O_3, and 17 mol% SiO_2. The melt's high water content necessitates Fe enrichment to achieve neutral buoyancy, which can only be sourced from Fe-rich heterogeneities ($Fe^{\#}$ = 100Fe/(Mg+Fe) in mole; $Fe^{\#}$ >18) within the MTZ. In contrast, melts derived from normal MTZ material ($Fe^{\#}$ <18) remain buoyant and migrate upward, precluding stable layer formation. We conclude that global dehydration melting generates hydrous melts, but only Fe-rich heterogeneities enable melt retention, reconciling the coexistence of widespread LVL detections and their lateral discontinuities.

incipient melt | low velocity zones | 410 km discontinuity | fast cooling | multi-anvil apparatus

Significance

The composition of incipient hydrous melt is critical for understanding the origin of low-velocity zones observed at the bottom of the upper mantle, mantle dynamics, chemical reservoirs, and the deep mantle water cycle. By developing a fast-quenching cell assembly for high-pressure experiments, we addressed long-standing challenges in accurately analyzing melt composition due to sample heterogeneity and determined the incipient hydrous melt's composition at the bottom of the upper mantle. The incipient melt is highly enriched in water, necessitating elevated Fe content to achieve a density comparable to or exceeding that of the surrounding mantle. This study demonstrates that global dehydration melting generates hydrous melts, but only Fe-rich heterogeneities enable melt retention.

Sporadic seismic low-velocity layers (LVLs) and associated high electrical conductivity layers detected globally above the 410 km discontinuity (D410) (1–10) are frequently interpreted as evidence of hydrous silicate melt (hereafter referred to as "410 melt") (11, 12). However, the lateral discontinuity of these layers has fueled a decades-long debate over whether such melt layers originate from localized or global processes. Localized mechanisms—such as dehydration of subducted slabs (1) or hydrous mantle plume interactions (10)—explain spatial sparsity but fail to account for the global occurrence of LVLs. Conversely, global models invoking dehydration melting near the D410 via the hydrous wadsleyite-to-olivine transition (11, 12) or decreasing water solubility in ascending olivine (12) align with widespread detections but conflict with the intermittent distribution of LVLs. A unifying hypothesis could be that 410 melt forms globally but is preserved only where melt mobility and stability permit retention.

The global genesis of 410 melt has been investigated through geophysical observations and high-pressure experiments. Seismic data reveal no correlation between LVL detections and tectonic settings, implying a universal controlling mechanism (2, 8). Dehydration melting is inevitable if the MTZ's water content exceeds the upper mantle's solubility. While localized MTZ regions exhibit water concentrations up to ~1.4 wt% [evidenced by hydrous ringwoodite inclusions in diamonds (13)], global estimates vary widely: ranging from 1,000 ppm to ~1 wt%, roughly corresponding to ~0.8-7.6 mol%, based on magnetotelluric observation, mantle rheology, and mineral physics (14–16). We note that a recent geomagnetic diurnal variation study reported a water content ~300 ppm (~0.24 mol%) (17), yet recalibration using alternative conductivity data yields ~1,000 ppm (~0.24 mol%) in the same study (17). Collectively, these studies suggest a global MTZ water content likely ≥1,000 ppm (~0.8 mol%), with local heterogeneities reaching 1 wt%. In contrast, the upper mantle's water solubility decreases from 600–1,000 ppm (~0.48–0.8 mol%) at 410 km (11, 12, 15, 18) to 400–600 ppm (~0.32–0.48 mol%) at ~300 km depth (12, 18). These estimates suggest that MTZ water content (likely ≥1,000

Author contributions: L.X. and H.K.M. designed research; L.X., N.M., and T.Q. performed research; T.K. and N.M. contributed new reagents/analytic tools; L.X. analyzed data; L.X. wrote the first draft of paper; all authors revised the paper.

Reviewers: N.B., Laboratoire Magmas et Volcans, France; D.N., Università degli studi di Padova, Italy; and X.Y., Nanjing University.

The authors declare no competing interest.

Copyright © 2025 the Author(s). Published by PNAS. This article is distributed under Creative Commons Attribution-NonCommercial-NoDerivatives License 4.0 (CC BY-NC-ND).

[1]To whom correspondence may be addressed. Email: longjian.xie@hpstar.ac.cn or maohk@hpstar.ac.cn.

This article contains supporting information online at https://www.pnas.org/lookup/suppl/doi:10.1073/pnas.2500017122/-/DCSupplemental.

Published June 5, 2025.

Downloaded from https://www.pnas.org by WUHAN UNIVERSITY on June 23, 2025 from IP address 218.197.145.100.

ppm) exceeds the upper mantle's capacity, implying that dehydration melting likely occurs globally near D410.

Long-term preservation of the 410 melt layer requires melt density to exceed that of the surrounding mantle (11, 19). A critical barrier to validating the unifying hypothesis lies in the poorly constrained composition of 410 melt, particularly its water and iron (Fe) content, which introduce large uncertainties in melt density estimations. The 410 melt is expected to be the incipient hydrous melt of mantle peridotite near the D410 (20–23). A direct measurement of low-degree melt (2 wt%) in hydrous peridotite suggests compositions of 16.4 mol% FeO and 42 mol% H_2O (24). However, these results may suffer from disequilibrium artifacts, limited melt volume for analysis, and quenching-induced crystallization (12). Indirect methods yield conflicting estimates: Matsukage et al. (19) estimated a melt with 7.6 mol% FeO and 15.7 mol% H_2O from high-degree melting experiments (>10 wt% melt), while Fe-free systems (e.g., MgO–SiO_2–H_2O) predict H_2O contents >40 mol% (20, 21, 23).

To address disequilibrium and low melt-volume challenges, an iterative method, which iteratively adjusts the input melt to achieve equilibrium with source peridotite (25, 26), has been developed to determine the composition of the mantle's incipient melt. However, hydrous low-degree melts quenched at the bottom of upper mantle pressures often crystallize into coarse grains (~200 μm) (20, 25), hindering accurate melt analysis via electron microprobe (EPMA) or laser ablation inductively coupled plasma mass spectrometry (LA-ICP-MS). This limitation impedes the application of this method for precise determination of the 410 melt composition.

In this study, we developed a fast-quench technique to preserve hydrous peridotite melts at near-D410 pressures as glass or fine-grained quench crystals. By integrating this technique with the iterative method, we precisely determined the 410 melt composition. Using these results, we investigated the stability and fate of the 410 melt.

1. Fast-Quenching Design and 410 Melt Composition

To investigate the composition of 410 melt, we developed a high-pressure cell assembly optimized for rapid quenching. The design employs two diamond powder pistons positioned at both ends of the capsule to increase the quench rate of sample (*SI Appendix*, Fig. S1*B*; see *Materials and Methods* for specifications), enabling preservation of hydrous peridotitic melts as glass (for systems with ≤14 mol% H_2O; *SI Appendix*, Figs. S2–S5) or as fine crystalline phases (<5 μm grain size; Fig. 1) at pressures exceeding 10 GPa.

Using this assembly, we conducted iterative equilibration experiments in a CaO–MgO–FeO–Al_2O_3–SiO_2–H_2O system at 13 GPa and 1,527 °C to determine the composition of incipient melts near D410 (see *Materials and Methods* for details). Temperatures were monitored in situ using a W-Re thermocouple, with spatial variations within the sample constrained to <40 °C via calibration using a spinel layer growth thermometer (27). Pressure was estimated using the pressure-load curve for the same cell assembly at 1,500 °C.

Starting with an initial melt composition inferred from Matsukage et al. (19), iterative equilibration with pyrolite rapidly converged to a melt composition of 43.4 mol% H_2O, 9.7 mol% CaO, 26.2 mol% MgO, 4.4 mol% FeO, 0.2 mol% Al_2O_3, and 16 mol% SiO_2 (*SI Appendix*, Table S4 and Fig. S11). Subsequent iterations revealed a minor compositional evolution, characterized by a gradual increase in FeO (4.4 → 4.5 mol%) and decrease in MgO (26.2 → 25.2 mol%) (*SI Appendix*, Table S4 and Fig. S11).

At convergence, five coexisting phases were identified: olivine (ol), garnet (gt), Ca-rich clinopyroxene (Ca-cpx), Mg-rich clinopyroxene (Mg-cpx), and melt (Fig. 1). In this six-component system, one degree of freedom remains unconstrained. Olivine equilibrated with the incipient melt exhibits a lower $Fe^{\#}$ [$Fe^{\#}$ = 100*Fe/(Fe+Mg); $Fe^{\#}$ = ~8] than pyrolitic olivine ($Fe^{\#}$ ~10), indicating that the unresolved variable is related to the melt's $Fe^{\#}$. If we combine the MgO and FeO into a single component [(Mg,Fe)O], the average converged melt composition, with 43 mol% H_2O, 9.2 mol% CaO, 30.5 mol% (Mg,Fe)O, 0.2 mol% Al_2O_3, and 17 mol% SiO_2 (*SI Appendix*, Table S4), represents a pseudoeutectic composition in the CaO–(Mg,Fe)O–Al_2O_3–SiO_2–H_2O system. The pseudoeutectic nature of 410 melt indicates that its water content (~43 mol%) is insensitive to the initial water content of the MTZ, provided that sufficient water is present to initiate dehydration melting near the D410. This derived H_2O content is consistent with predictions from Fe-free systems (20, 21, 23) and direct measurements of low-degree melts (24) but higher than the high-degree melt models (19). The consistency of H_2O content between Fe-bearing and Fe-free systems further confirms that the unconstrained variable is primarily related to the melt's $Fe^{\#}$, rather than its water content. To reflect the pseudoeutectic character of the 410 melt, we report the incipient melt composition with (Mg,Fe)O treated as a combined component.

The Fe content in 410 melt can vary across a wide range, controlled by the initial Fe content of the source rock and the Fe-Mg exchange coefficient between the melt and coexisting solids, defined as $K^{Fe}_{m\text{-}s} = Fe^{melt} * Mg^{solid}/(Mg^{melt} * Fe^{solid})$ in mole fraction. To investigate the influence of source-rock Fe content, we analyzed the Fe-Mg exchange coefficients between the incipient melt and coexisting phases (*SI Appendix*, Table S5). Using these coefficients, we estimated the bulk Fe-Mg exchange coefficient between the melt and undepleted mantle peridotite (UMP), a composition similar to pyrolite (28), by weighted averaging of each melt-mineral $K^{Fe}_{m\text{-}s}$ based on their modal proportions in UMP, yielding a value of 2.47 (*SI Appendix*, Table S5). This result lies between previously reported values at 6 GPa ($K^{Fe}_{m\text{-}s}$ =2.9 to 3.4; ref. 25) and 24 GPa ($K^{Fe}_{m\text{-}s}$ = 2.0; ref. 29), suggesting a systematic decrease in Fe-Mg extrange coefficients with increasing pressure. For reference, we also report the partitioning coefficient, defined as $D^{Fe}_{m\text{-}s} = Fe^{melt} * (Mg + Fe)^{UMP}/[(Mg + Fe)^{melt} * Fe^{UMP}]$ in mole fraction, which is another frequently used parameter reflecting Fe partitioning. This yields a value of 2.04 (*SI Appendix*, Table S5).

2. Near-Identical $Fe^{\#}$ between the MTZ and UMP

D410, marking the boundary between the upper mantle and MTZ, is attributed to the pressure-induced polymorphic transformation of olivine into wadsleyite (30). As schematically illustrated in Fig. 2, the downward injection of cold slabs into the MTZ or even into the lower mantle (LM) drives broad background upwelling (11). In the upwellings, a back-transition from wadsleyite to olivine occurs at D410. Geophysical and laboratory studies demonstrate that wadsleyite in the MTZ likely contains water exceeding the solubility limit of olivine (14–16, 18), leading to dehydration melting during this transition. Furthermore, melting continues at shallower depths due to the decreasing water solubility in olivine (12). The generated melt percolates downward to the D410 if its density exceeds that of the ambient mantle, or upward toward the surface if it is less dense. The residual solids serve as the source material for mid-ocean ridge basalts.

The UMP is widely recognized as the source material for mid-ocean ridge basalts (28). Using our melt-UMP Fe-Mg extrange

Downloaded from https://www.pnas.org by WUHAN UNIVERSITY on June 23, 2025 from IP address 218.197.145.100.

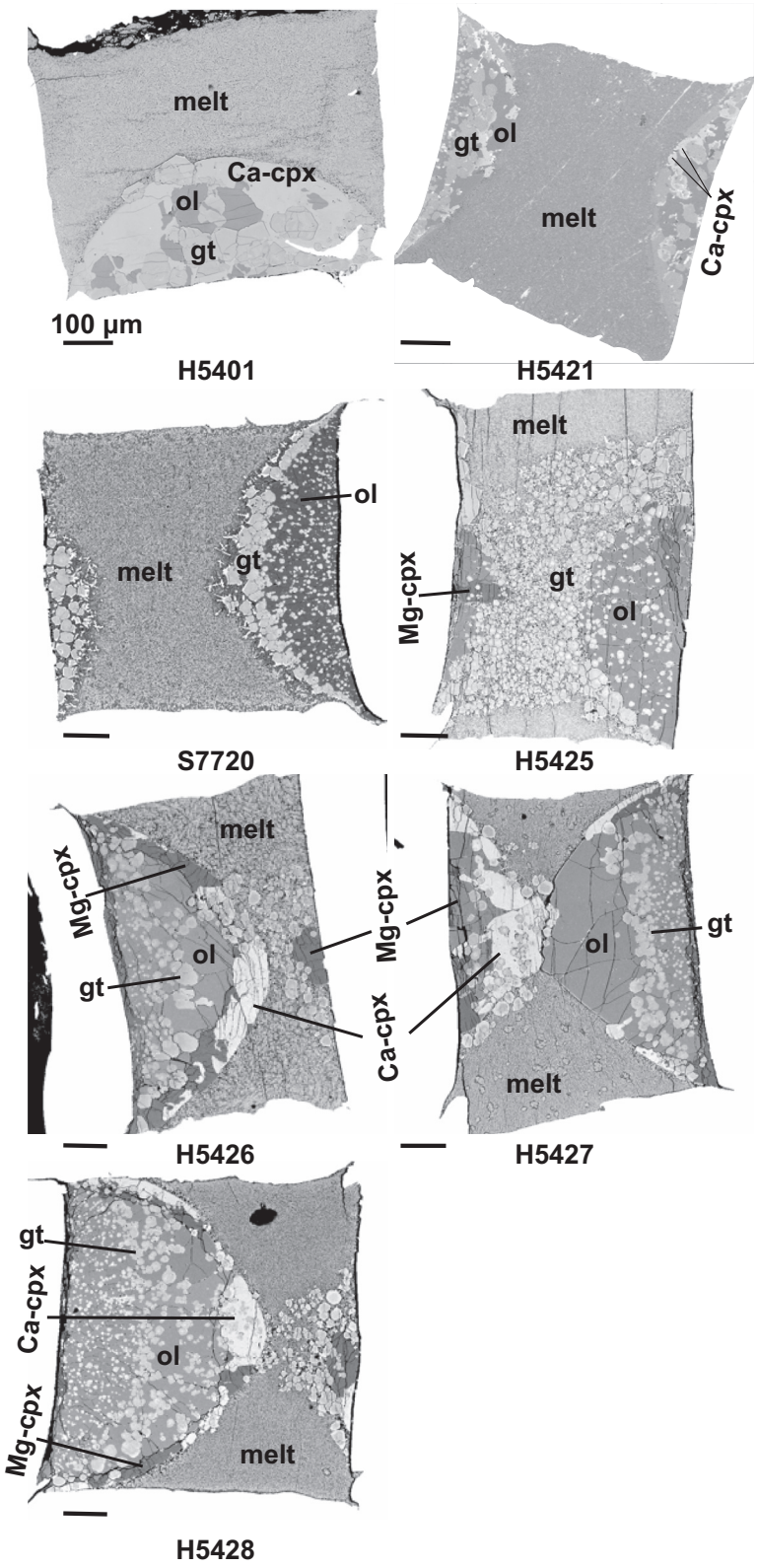

Fig. 1. Backscattered electron (BSE) images of the recovered samples of iteration experiments. ol: olivine; gt: garnet; Ca-cpx: Ca-rich clinopyroxene; Mg-cpx: Mg-rich clinopyroxene.

coefficient, the MTZ's Fe content can be reconstructed from UMP's composition by adding back the removed melt (*Materials and Methods*). As a larger fraction of melt (F), is added back, the resulting $Fe^{\#}$ of MTZ and coexisting melt increases (Fig. 3). The fraction of melt removed during the formation of UMP can be estimated based on the mass balance of H_2O, whose content in 410 melt is near-constant in mole fraction. The maximum fraction (F_{max}) is constrained by assuming that UMP is completely dry and all MTZ water is consumed to form 410 melt. Using the mass balance equation, F_{max} is calculated as the ratio of water content between the MTZ and 410 melt (H_2O^{MTZ}/H_2O^{melt} in moles). The MTZ contains 0.1 to 1 wt% H_2O (14–16), roughly corresponding

Downloaded from https://www.pnas.org by WUHAN UNIVERSITY on June 23, 2025 from IP address 218.197.145.100.

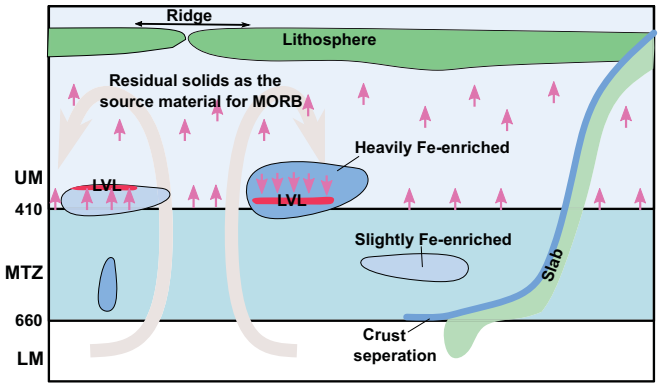

Fig. 2. Schematic of dehydration melting and low-velocity layer (LVL) formation during slab subduction-induced mantle upwelling. Subduction of oceanic slabs into the mantle transition zone (MTZ) or lower mantle (LM) drives large-scale passive upwelling (thick mustard-yellow arrow). Dehydration melting initiates at the D410 via pressure-induced breakdown of hydrous wadsleyite to olivine, followed by continued melting at shallower depths due to decreasing water solubility in olivine. Resulting melts either accumulate as LVLs in the deep upper mantle (UM) or migrate toward the surface (purple arrows). Residual solids constitute the source material for mid-ocean ridge basalt (MORB) generation. Partial crustal separation of the subducted slab within the MTZ facilitates mixing between recycled oceanic crust and ambient mantle, forming Fe-enriched domains. LVLs preferentially develop in these Fe-enriched heterogeneities while remaining absent in normal mantle compositions.

to ~0.3 to 2.7 mol%, while 410 melt has ~43 mol% H_2O. F_{max} reaches 0.063 at the upper limit (2.7 mol % H_2O). Even under this extreme condition, the MTZ $Fe^{\#}$ is calculated as 11.3, slightly higher than UMP's $Fe^{\#}$ (~11.0). As melt is extracted from the MTZ material, the $Fe^{\#}$ of the MTZ material decreases from 11.3 to 11.0, and the $Fe^{\#}$ of the coexisting melt decreases from 24 to 23. Consequently, the $Fe^{\#}$ of the 410 melt, from initial melting to the final stage of forming UMP-like composition, is estimated to be 23.5 ± 0.5. The pseudoeutectic melt composition with this $Fe^{\#}$ yields an averaged 410 melt composition of 43 mol% H_2O, 9.2 mol% CaO, 7.2 mol% FeO, 23.3 mol% MgO, 0.2 mol% Al_2O_3, and 17 mol% SiO_2.

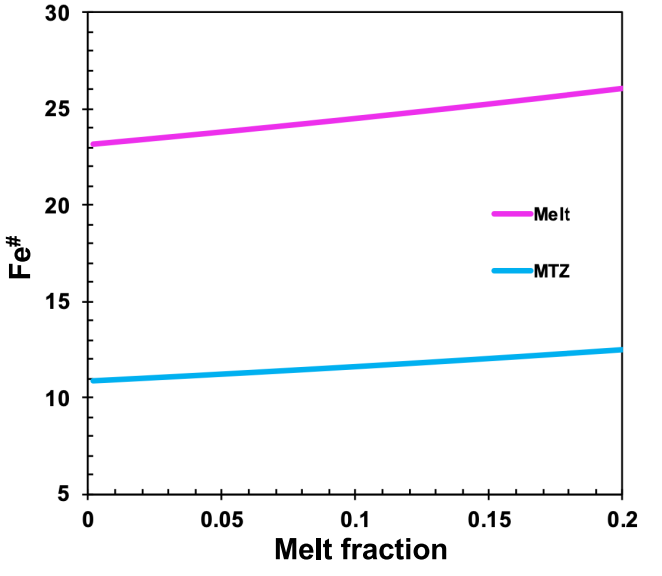

Fig. 3. Evolution of $Fe^{\#}$ in MTZ and coexisting melt as a function of the cumulative melt fraction added back to a UMP composition. The procedure for adding back the melt is detailed in *Materials and Methods*. Cumulative melt fraction represents the total fraction of melt added to reconstruct the composition of the MTZ.

3. Preservation Challenges of 410 Melt Generated by a Normal MTZ

The stability of the 410 melt layer depends critically on its density relative to the surrounding upper mantle. If the melt has a higher density than the upper mantle rock but lower than the MTZ rock, the melt can stay atop the MTZ. However, if it is less dense than the upper mantle rock, the melt cannot form a melt layer atop the MTZ. The equation of state from Drewitt et al. (21) suggests that a 410 melt with 43 mol% H_2O has to have $Fe^{\#}$ >35 to match or exceed the density of upper mantle rock (Fig. 4*B*). However, melts forming atop the MTZ have a $Fe^{\#}$ <25. Therefore, the melt cannot stay at the top of the MTZ and migrate upward. This upward migration precludes stable melt-layer preservation atop D410 but facilitates MTZ water cycling—complementing slab subduction—and provides a metasomatic agent for the lithosphere upper mantle (12).

4. Stable Melt Layers from Fe-Rich Heterogeneities

The density of the melt increases with decreasing water content or increasing Fe content (Fig. 4). For a melt density to exceed that of the surrounding upper mantle, the water content of the melt must be lower or its Fe content must be higher than the above-mentioned estimates. However, the water content of 410 melt (~43 mol%) is controlled exclusively by pressure and temperature but independent of the MTZ composition. Therefore, the melt density cannot be adjusted by the water content. In contrast, the Fe content can vary significantly due to MTZ heterogeneity, offering a viable mechanism for melt stabilization.

Elevated Fe content increases the density of both the residual solid and the resultant melt, altering melt migration dynamics in the upper mantle. The fate of the melt depends on the density contrasts among the melt, the residual solid, and the surrounding upper mantle (Fig. 2). When the melt is less dense than the surrounding mantle, it ascends toward the surface. When the melt density lies between that of the surrounding mantle and the residual solid, it ponds at the top boundary between the residual solid and the surrounding mantle. When the melt density exceeds that of the residual solid but remains lower than the MTZ, it accumulates atop the D410. Consequently, stable melt layers form only when the melt density surpasses that of the surrounding normal mantle. Source rocks with $Fe^{\#}$ > 18 produce melts with $Fe^{\#}$ > 35, which achieve densities exceeding that of the surrounding upper mantle (Fig. 4).

Importantly, elevating Fe content within a reasonable range has negligible effects on dehydration melting near the D410. Fei et al. (31) demonstrated that water solubility in wadsleyite remains nearly constant across a range of $Fe^{\#}$ values (10 to 25), indicating minimal changes in MTZ water solubility when $Fe^{\#}$ increases from 10 to 18. Although increased water solubility in olivine with increasing $Fe^{\#}$ has been observed at low pressures (≤6 GPa) (32), Fei et al. (33) compiled experimental data showing that Fe has little influence on water solubility in olivine near the D410. Consequently, elevating Fe content provides a robust mechanism for stabilizing melts without significantly altering dehydration melting processes.

One candidate for Fe-rich source rocks is heterogeneities associated with subducted oceanic crust. Oceanic crust, with $Fe^{\#}$ values as high as ~40 (34), can be subducted and entrained into the MTZ (35, 36). The accumulation of the oceanic crust in MTZ, likely resulting from the segregation of basaltic crust and depleted mantle within subducted slabs, has been both proposed and seismically

Downloaded from https://www.pnas.org by WUHAN UNIVERSITY on June 23, 2025 from IP address 218.197.145.100.

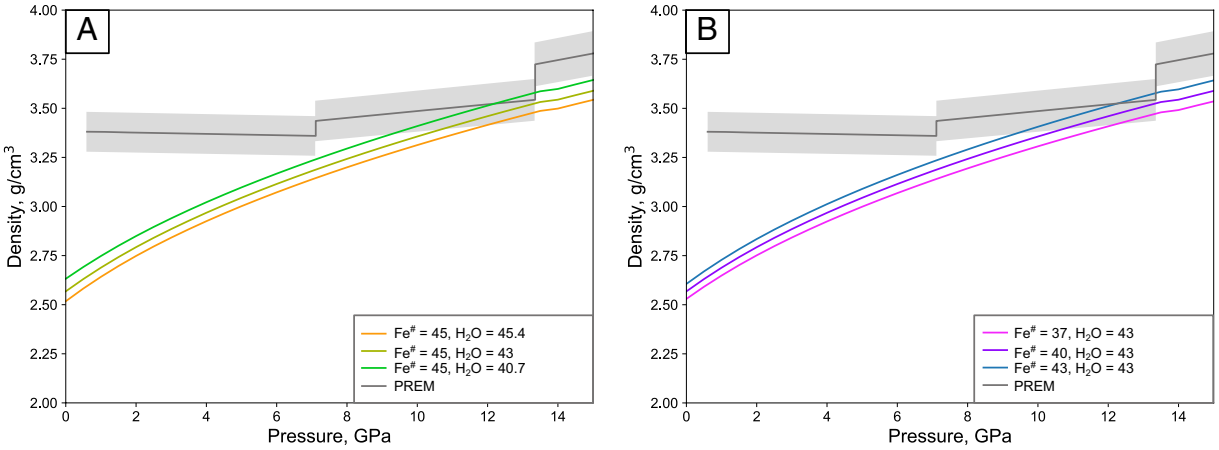

Fig. 4. Density of the incipient melt with slight variation of water content (*A*) and Fe/(Fe+Mg) ratio (*B*). The gray envelope indicates 3% uncertainty of the PREM model. The density was calculated based on the equation of state from Drewitt et al. (21). $Fe^{\#}$ denotes 100*Fe/(Fe+Mg) in mole.

detected (37–40). Notably, a recent global seismic study provides compelling evidence for widespread basalt accumulation in the MTZ (39). Mixing such basaltic material with ambient mantle (e.g., pyrolite with $Fe^{\#}$ ~ 10) generates heterogeneities spanning $Fe^{\#}$ = 10 to 40. Among these, heterogeneities with $Fe^{\#}$ >18 represent viable source rocks capable of producing stable melt layers atop the D410.

5. Conclusiovns

Dehydration melting likely occurs globally near D410 due to the MTZ's water content (≥1,000 ppm) exceeding the upper mantle's capacity (<1,000 ppm), explaining the global detection of LVLs atop D410. Our high-pressure experiments demonstrate that the 410 melt is highly hydrous (43 mol%) and its water content remains nearly invariant along the geotherm. As a result, only melts derived from Fe-enriched source rock ($Fe^{\#}$ > 18) achieve sufficient density to form long-lived stable layers atop the D410. In contrast, melts generated in a normal MTZ region ($Fe^{\#}$ < 18) migrate upward due to buoyancy, resulting in the discontinuities of the detected LVLs. Therefore, while 410 melt forms globally, melts only derived from Fe-enriched heterogeneities are preserved as stable melt layers, reconciling the coexistence of global LVL detections and their lateral discontinuities (2, 8, 9). Since the equations of state used for hydrous melt in this study suffer from significant uncertainties, improved models are critical to accurately constrain the Fe and water contents required for melt neutrality in future studies.

6. Materials and Methods

6.1. High-Pressure-temperature Experiments.

6.1.1. Designing the fast-cooling assembly. Based on high-degree melting experiments (>10 wt%) on hydrous pyrolite, Matsukage et al. (19) suggested that the 410 melt composition contains 5 wt% H_2O (corresponding to 13.4 mol%), with the dry composition referred to as M05 hereafter (*SI Appendix*, Table S6). We initiated this study by conducting high-pressure melting experiments on M05 with 5 wt% H_2O in a 10/4 (edge-length of octahedron/edge-length of anvil truncation) cell assembly (*SI Appendix*, Fig. S1*A*) to determine its liquidus temperature. To test the possible reaction between diamond and hydrous silicate melt, we introduced a diamond powder layer into the sample. In this experiment, we accidentally obtained bright glassy phase patches (*SI Appendix*, Fig. S2*A*), confirmed via EBSD and TEM analysis (*SI Appendix*, Fig. S2 and S3), among the quenched crystals. These patches likely resulted from the enhanced quench rate facilitated by the diamond layer.

Inspired by this observation, we designed a fast-quenching cell assembly using two diamond pistons at the ends of the capsule (*SI Appendix*, Fig. S1*B*). A platinum (Pt) capsule was employed to isolate the melt from the diamond pistons and surrounding materials, preventing potential contamination. To validate the design, we performed over five experiments on the model 410 melt composition of M05 with 5 wt% H_2O at 15 GPa. All recovered samples showed bright glassy patches embedded within quenched crystals (*SI Appendix*, Fig. S5), demonstrating the rapid cooling capability of the cell. The glassy nature of the patches was confirmed by electron backscattered diffraction (EBSD) analysis or transmission electron microscopy (TEM) (*SI Appendix*, Figs. S2–S4).

We implemented this design in 10/4, 10/5, and 7/3 assemblies. In all the assemblies, Cr-doped MgO (5 wt% Cr_2O_3) octahedra were used as pressure media. Ha08 tungsten carbide cubes were used as second-stage anvils for the 10/4 and 10/5 cell assembly, while Ha06 cubes were used for the 7/3 cell assembly. $LaCrO_3$ was used as the heating element for all the cell assemblies. Pt capsules with two ends welded for sealing were used for melting experiments. Temperatures were monitored by $W_{75}Re_{25}$-$W_{97}Re_3$ thermocouples with 0.13 or 0.05 mm in diameter. All the high-pressure, high-temperature conditions were generated using Kawai-type multianvil presses at the Bayerisches Geoinstitut, University of Bayreuth, Germany.

The cell assemblies were first compressed to the target load at room temperature over a period of more than 180 min, and then heated to the desired temperature under constant load at a rate of ~50 K/min. After heating, quenching was performed by cutting off the power. After quenching, samples were decompressed and recovered. Recovered samples were polished for subsequent textural, phase, and chemical analysis.

6.1.2. Characterizing the fast-cooling design. The pressure-load curve of 10/4 cell with the fast-cooling design was calibrated using the phase transitions of coesite to stishovite and forsterite (Fo) to wadsleyite (Wd) at 1,500 °C (*SI Appendix*, Fig. S6). The temperature distribution in the sample area was calibrated using a spinel layer growth thermometer (27). The temperature is 1,550 ± 20 °C within the 1 mm diameter cylinder at the cell center when the thermocouple reading was 1,500 °C (*SI Appendix*, Fig. S7).

The cooling rates of various cell assemblies were studied by monitoring the temperature changes during quenching using a fast-recording system. The temperatures during quenching were recorded with a Thermo-Amplifier-Box, capable of logging up to 1,000 temperature values per second (41). Compared to a cooling rate of ~650 °C/s for normal multianvil assembly (41), the cooling rate of our design was increased to 2,000 to 5,300 °C/s (*SI Appendix*, Table S2), depending on the cell assembly, pressure, and sample phases during quenching (*SI Appendix*, Table S2 and Figs. S8 and S9). The smaller cell has a higher cooling rate, probably due to the shorter length required to conduct heat to the anvil top. Pressure slightly increases the cooling rate, probably due to reduced thermal inertia as a result of reduced volume of the pressure medium and enhanced thermal coupling. Note that the cell containing a Fo + Wd in the recovered sample exhibited a significantly lower cooling rate compared to pure Wd or Fo samples

Downloaded from https://www.pnas.org by WUHAN UNIVERSITY on June 23, 2025 from IP address 218.197.145.100.

at similar pressures. This may be due to the latent heat of the Fo-Wd phase transition at ~1,500 °C during quenching. Similarly, samples containing a mixture of melt and crystals are expected to have a lower cooling rate than those with pure melt or pure crystals, which explains why the largest glass is obtained in Run H5382 at 1,900 °C.

6.1.3. Starting material for melting experiments. The starting materials were mixtures of oxides and hydroxides. Reagent-grade powders of SiO_2 (purity >99%), Al_2O_3 (>99%), MgO (>99%), FeO (>99%), $Mg(OH)_2$ (>95%), $Al(OH)_3$ (>95%), $Ca(OH)_2$ (>95%), and silica gel (>99%) were mixed in an appropriate ratio (*SI Appendix*, Table S4) and hand-ground with an agate mortar and pestle. The purity of oxides and silica gel used is higher than 99%, while the purity of hydroxides is higher than 95%. Water was incorporated into the mixtures through the addition of $Ca(OH)_2$, $Mg(OH)_2$, $Al(OH)_3$, and silica gel in sequence until the desired water content was achieved. For the compositions of melt-6 and melt-7 in *SI Appendix*, Table S4, silica gel was required as an additional water source because the desired water content could not be achieved even when all Ca, Mg, and Al were added as hydroxides. The water content in silica gel was determined by measuring the weight loss after heating to 1,000 °C.

6.1.4. Iteration experiments. We applied the fast-quench design of the 10/4 cell assembly to determine the 410 melt composition using an iterative method. The core concept of this method is to equilibrate an estimated melt composition with a fertile peridotite (pyrolite) composition (roughly 1:1 in volume) at 13 GPa, progressively refining the melt composition until minimal reactions occur between pyrolite and the estimated melt. At each iteration, solid-melt reactions take place if the estimated melt composition deviates significantly from equilibrium with pyrolite, resulting in a new melt composition that is closer to equilibrium. This updated melt composition is then used as the guessed melt for the next iteration. The first iteration involves establishing an initial guessed melt composition. The modeled composition from Matsukage et al. (19) is a good candidate. Based on the initial melting experiments in this study (*SI Appendix*, Fig. S5 and Table S1), the M05 composition with 5 wt% H_2O requires temperatures exceeding 1,800 °C to fully melt (*SI Appendix*, Table S1), which is ~300 °C higher than the geotherm. Therefore, we used a M05 composition with 10 wt% H_2O for the first equilibrium experiment. In the initial trials, several samples were heated to and maintained at 1,527 °C for 10 to 20 min. However, solid and melt sometimes failed to reach equilibrium and to separate completely, which is crucial for preventing quench-related modifications and for accurate chemical analysis. To address this, all the later iterations used a two-step heating process to improve equilibrium and separation. Samples were first heated to 1700–1800 °C and held for 3 min, followed by cooling to 1,527 °C and maintained for 20 to 30 min.

To determine the solid phases coexisting with the melt, we attempted to determine the mineral assemblages of dry pyrolite by conducting a subsolidus experiment at 13 GPa and 1,527 °C for 24 h. However, equilibrium was not achieved due to slow reaction kinetics, as indicated by the recovered sample (*SI Appendix*, Fig. S10). In this experiment, we roughly identified ol, gt, and Ca-cpx as the primary coexisting phases. However, the solid phases coexisting with the melt in the final iteration run were olivine (ol), garnet (gt), Ca-rich clinopyroxene (Ca-cpx), and Mg-rich clinopyroxene (Mg-cpx) (Fig. 1). This difference is likely due to the difficulty of achieving phase equilibrium in dry samples, whereas the hydrous melt in our experiments promotes equilibrium, as indicated by the large, straight-boundary crystals of Ca- and Mg-cpx. Mass balance calculations reveal that UMP, a composition similar to pyrolite (28), comprises ~51% ol, 34% gt, 6% Ca-cpx, and 8% Mg-cpx (mol%). Since melt facilitates equilibrium, we conclude that Mg-cpx should be one of the coexisting solid phases at least to 13 GPa (Fig. 1 and *SI Appendix*, Table S3), 3 GPa higher than previously reported (42).

6.2. Glass Identification by EBSD or TEM Analysis. Two methods were used to determine whether the bright patches in the quenching crystals were glass or not. The first method is the Electron Backscatter Diffraction (EBSD) analysis. The recovered samples were impregnated by epoxy and polished with Buehler™ Minimet 1,000 with diamond paste of progressively finer grit size from 15 μm to 0.25 μm. Colloidal silica was applied to the polisher for final polishing because the sampling depth is less than 1 μm for EBSD analysis. After the polishing, the surface was coated with carbon with about 5-nm thickness. Forescattered electron (FSE) imaging and EBSD were conducted with a Zeiss Gemini™ 300 field emission scanning electron microscope (SEM) in the Department of Materials Science and Metallurgy, University of Cambridge. In the SEM vacuum chamber, the polished surface was tilted by 70°. FSE images were acquired at an accelerating voltage of 20 kV, with an aperture 120 μm in diameter, at a working distance of 15 mm. EBSD was conducted under the same conditions with 1 μm step size by a Symmetry™ EBSD detector and AZtec™ 4 acquisition software from Oxford Instruments™. A linear scan of EBSD was conducted across the quenching crystals and bright patch. A patch is identified as glass if it shows a diffused diffraction pattern EBSD analysis, while adjacent regions showed clear Kikuchi patterns (*SI Appendix*, Fig. S2 *C* and *D*).

The other method is TEM analysis. We performed the scanning transmission electron microscopy (STEM) imaging and chemical analyses on a field emission scanning transmission electron microscope (FEI, Titan G2 80–200 S/TEM), equipped with an energy dispersive X-ray spectrometer (EDS, 4 Silicon drift detectors, Bruker Quantax) in order to observe and analyze the chemical compositions of the quenched S7592 samples. For the TEM sample preparation, we used a focused ion milling machine (FEI Scios DualBeam milling). The TEM thin foils were a thickness of about 150 nm. To identify crystalline or amorphous states in the S7592 sample, selected area electron diffraction (SAED) patterns were investigated with conventional TEM images. Phases showing a diffuse Halo ring are identified as a glassy phase (*SI Appendix*, Fig. S3*C*). The STEM-EDS maps were taken at a resolution of 14 nm per pixel and dwell time 16 μsec using a subnanometer-sized electron beam with 0.06 nA probe current at 200 kV-acceleration voltage. To accumulate statistically enough characteristic X-ray counts in a quantitative EDS map, the total acquisition time was 3,600 s in live time with a count rate of 1.3 kcps. During the acquisition, an image drift correction function was always activated to prevent artifacts in the profile. To get quantitative compositions of the samples, we corrected Z-number with calibrated k-factors using a natural pyrope garnet (43) and absorption effects on the evaluations of EDS spectrum (44, 45). The glassy patch and the quenched crystals showed the same average composition, indicating that the glass represents the same melt as the quenched crystals prior to solidification.

6.3. Chemical Analysis of Recovered Samples By Electron Microprobe. While previous studies have reported quenched crystal grain sizes of approximately 200 μm (25), the crystals in our experiments exhibit significantly finer grain sizes, typically smaller than 5 μm, even in samples with water contents up to 20 wt% (Fig. 1). This smaller grain size is ideal for averaging the composition of quenched crystals using Electron Probe Micro-Analysis (EPMA) with a diffused beam.

The compositions of recovered samples were measured by EPMA at Bayerisches Geoinstitut, University of Bayreuth, Germany. Standards used for calibration included Re, Pt, Fe, diopside, spinel, and enstatite. Measurements were conducted at an accelerating voltage of 15 kV. For solid phases and metallic capsules, a beam size of 1 μm was employed. For the melt composition in melt regions, a defocused beam (10 or 20 μm) was combined with rectangular scanning (typically 40 × 40 to 100 × 100 μm) using a step size equal to the beam size to obtain an average composition. The measured composition of nonvolatile elements is representative of the melt before quenching. Although our fast-cooling assembly preserved melts as glass for systems with $H_2O \leq 5$ wt%, melts in the iteration experiments, containing ~10 wt% H_2O or more, crystallized into fine-grained crystals (typically <5 μm) rather than glass during quench. To quantify the water content of these high-H_2O melts, we employed the EPMA deficit method, which estimates original melt H_2O by reconciling analytical shortfalls in oxide totals. This approach provides reliable H_2O values with an error margin of ~2 wt% (29). An additional source of error arises from the assumption that all iron oxides are present as FeO, while some Fe_2O_3 component may exist. However, since the FeO content is less than 10 wt%, the maximum error introduced by this factor is less than 1 %. Consequently, the total error for the EPMA deficit method is less than 3 wt%.

6.4. Calculation of $Fe^{\#}$ in MTZ as a Function of the Melt Fraction in Mole. Given the exceptionally high water content of the 410 melt, its viscosity is extremely low (~10 mPa·s) (21, 46, 47), enabling efficient melt percolation except at locations where the melt has neutral buoyancy. As a result, melt is continuously removed from the source rock as it forms, preventing re-equilibration with the residual solid. To account for this process, the melt must be added back incrementally. We employed an iterative approach to calculate the $Fe^{\#}$ in the MTZ as a function of the melt fraction (in molar percent) extracted to form the UMP composition. The procedure is as follows:

Downloaded from https://www.pnas.org by WUHAN UNIVERSITY on June 23, 2025 from IP address 218.197.145.100.

1. *Initial Composition:* Set the molar amount of Fe and Mg in the residual solids according to their ratio in the UMP composition and the molar amount of (Fe + Mg) of melt based on the 410 melt composition. Assign the initial amount of UMP to 1.
2. *Fe/Mg Ratio in the Melt:* Calculate the Fe/Mg ratio of the melt ($R^{m}_{Fe/Mg}$) based on the melt-to-residual solid exchange coefficient ($K^{m/Res} = 2.47$, as determined in this study) and the Fe/Mg ratio of the residual solids ($R^{Res}_{Fe/Mg}$): $R^{m}_{Fe/Mg} = K^{m/Res} * R^{Res}_{Fe/Mg}$.
3. *Fe and Mg amount in Melt:* Use $R^{m}_{Fe/Mg}$ and the molar amount of (Fe + Mg) in melt to calculate the molar amount of Fe and Mg in the melt.
4. *Add Back Melt Fraction*: Add a small fraction of the calculated melt composition (df, e.g., 0.001) back into the system.
5. *Recalculate System Composition:* Determine the total Fe and Mg content using the contributions from the residual solid (1) and the added melt (df).
6. *Update melt fraction:* Calculate the melt fraction as

$$\text{melt fraction} = \frac{\textit{total melt amount added}}{1 + \textit{total mel amount added}}.$$

7. *Update Fe#:* Calculate the Fe# for the system and the melt using their updated Fe and Mg amounts.
8. *Iterate:* Set the total Fe and Mg amounts calculated in the previous step as the starting composition of the residual solid for the next cycle. Repeat steps 2 to 7 until the desired melt fraction is reached.

6.5. Density Calculation of 410 Melt. The densities of 410 melt were calculated using the equation of state of a MgO–SiO_2–H_2O system (21). For the Fe effect, the density can be approximately calculated based on the difference in atomic mass of Fe and Mg (21). Similarly, the Ca effect was also calibrated according to the difference in atomic mass of Ca and Mg in this study.

Data, Materials, and Software Availability. All study data are included in the article and/or *SI Appendix*.

ACKNOWLEDGMENTS. We thank H. Fischer for cell assembly preparation, R. Njul for polishing the sample, D. Krauße for assistance in EPMA measurement, and D. Wiesner for the assistance in cutting the sample by FIB at Bayerisches Geoinstitut (Germany). We thank Dr. Michael Walter and Dr. Yingwei Fei at Earth & Planets Laboratory, Carnegie Institution for Science, US, for the suggestion on the iteration experiments on the composition determination of 410 melt. We thank Dr. David Wallis (University of Cambridge) for technical assistance with EBSD analysis. The Titan G2 TEM and the FIB at BGI (Bayerisches Geoinstitut) were financed by DFG Grants INST 91/251-1 FUGG and INST 91/315-1 FUGG). H.K.M. acknowledges financial support from Shanghai Key Laboratory Novel Extreme Condition Materials, China (No. 22dz2260800) and Shanghai Science and Technology Committee, China (No. 22JC1410300).

Author affiliations: [a]Center for High Pressure Science and Technology Advanced Research (Shanghai), Shanghai 201203, China; [b]Bayerisches Geoinstitut, University of Bayreuth, Bayreuth 95440, Germany; [c]Department of Earth Sciences, University College London, London WC1E6BS, United Kingdom; and [d]Shanghai Key Laboratory of Material Frontiers Research in Extreme Environments, Institute for Shanghai Advanced Research in Physical Sciences, Shanghai 201203, China

1. J. Revenaugh, S. A. Sipkin, Seismic evidence for silicate melt atop the 410-km mantle discontinuity. *Nature* **369**, 474–476 (1994).
2. B. Tauzin, E. Debayle, G. Wittlinger, Seismic evidence for a global low-velocity layer within the Earth's upper mantle. *Nat. Geosci.* **3**, 718–721 (2010).
3. K. Baba *et al.*, Electrical conductivity imaging of the Philippine Sea upper mantle using seafloor magnetotelluric data. *Phys. Earth Planet. Inter.* **183**, 44–62 (2010).
4. D. A. Toffelmier, J. A. Tyburczy, Electromagnetic detection of a 410-km-deep melt layer in the southwestern United States. *Nature* **447**, 991–994 (2007).
5. T.-R. Alex Song, Don V. Helmberger, S. P. Grand, Low-velocity zone atop the 410-km seismic discontinuity in the northwestern United States. *Nature* **427**, 530–533 (2004).
6. M. R. Agius, C. A. Rychert, N. Harmon, G. Laske, Mapping the mantle transition zone beneath Hawaii from Ps receiver functions: Evidence for a hot plume and cold mantle downwellings. *Earth Planet. Sci. Lett.* **474**, 226–236 (2017).
7. D. A. Thompson *et al.*, Hydrous upwelling across the mantle transition zone beneath the Afar Triple Junction. *Geochem. Geophys. Geosystems* **16**, 834–846 (2015).
8. S. S. Wei, P. M. Shearer, A sporadic low-velocity layer atop the 410 km discontinuity beneath the Pacific Ocean. *J. Geophys. Res. Solid Earth* **122**, 5144–5159 (2017).
9. G. Han *et al.*, Pervasive low-velocity layer atop the 410-km discontinuity beneath the northwest Pacific subduction zone: Implications for rheology and geodynamics. *Earth Planet. Sci. Lett.* **554**, 116642 (2021).
10. L. Vinnik, V. Farra, Low S velocity atop the 410-km discontinuity and mantle plumes. *Earth Planet. Sci. Lett.* **262**, 398–412 (2007).
11. D. Bercovici, S. Karato, Whole-mantle convection and the transition-zone water filter. *Nature* **425**, 39–44 (2003).
12. D. Andrault, N. Bolfan-Casanova, Mantle rain toward the Earth's surface: A model for the internal cycle of water. *Phys. Earth Planet. Inter.* **322**, 106815 (2022).
13. D. G. Pearson *et al.*, Hydrous mantle transition zone indicated by ringwoodite included within diamond. *Nature* **507**, 221–224 (2014).
14. T. Yoshino, T. Katsura, Electrical conductivity of mantle minerals: Role of water in conductivity anomalies. *Annu. Rev. Earth Planet. Sci.* **41**, 605–628 (2013).
15. S. Karato, Water distribution across the mantle transition zone and its implications for global material circulation. *Earth Planet. Sci. Lett.* **301**, 413–423 (2011).
16. H. Fei *et al.*, A nearly water-saturated mantle transition zone inferred from mineral viscosity. *Sci. Adv.* **3**, e1603024 (2017).
17. H. Zhang, G. D. Egbert, Q. Huang, A relatively dry mantle transition zone revealed by geomagnetic diurnal variations. *Sci Adv* **8**, eabo3293 (2022).
18. K. Zhang, L. Li, C. R. Stern, X. Yang, Water solubility of olivine under redox-controlled deep upper mantle conditions: Effects of pressure, temperature and coexisting fluids and implications. *Contrib. Miner. Petrol.* **180**, 9 (2025).
19. K. N. Matsukage, Z. Jing, S. I. Karato, Density of hydrous silicate melt at the conditions of Earth's deep upper mantle. *Nature* **438**, 488–491 (2005).
20. R. Myhill, D. J. Frost, D. Novella, Hydrous melting and partitioning in and above the mantle transition zone: Insights from water-rich MgO–SiO_2–H_2O experiments. *Geochim Cosmochim Acta* **200**, 408–421 (2017).
21. J. W. E. Drewitt, M. J. Walter, J. P. Brodholt, J. M. R. Muir, O. T. Lord, Hydrous silicate melts and the deep mantle H_2O cycle. *Earth Planet Sci Lett* **581**, 117408 (2022).
22. T. Inoue, Effect of water on melting phase relations and melt composition in the system Mg_2SiO_4–$MgSiO_3$–H_2O up to 15 GPa. *Phys. Earth Planet. Inter.* **85**, 237–263 (1994).
23. D. Novella *et al.*, Melting phase relations in the systems Mg_2SiO_4–H_2O and $MgSiO_3$–H_2O and the formation of hydrous melts in the upper mantle. *Geochim. Cosmochim. Acta* **204**, 68–82 (2017).
24. D. Freitas *et al.*, Experimental evidence supporting a global melt layer at the base of the Earth's upper mantle. *Nat. Commun.* **8**, 2186 (2017).
25. D. Novella, D. J. Frost, The composition of hydrous partial melts of garnet peridotite at 6 gpa: Implications for the origin of group II kimberlites. *J. Petrol.* **55**, 2097–2124 (2014).
26. M. M. Hirschmann, R. Dasgupta, A modified iterative sandwich method for determination of near-solidus partial melt compositions. I. Theoretical considerations. *Contrib. Miner. Petrol.* **154**, 635–645 (2007).
27. W. van Westrenen, J. A. Van Orman, H. Watson, Y. Fei, E. B. Watson, Assessment of temperature gradients in multianvil assemblies using spinel layer growth kinetics. *Geochem., Geophys., Geosystems* **4** (2003).
28. E. Jagoutz *et al.*, "The abundances of major, minor and trace elements in the Earth's mantle as derived from primitive ultramafic nodules" in *Proceedings of the 10th Lunar and Planetary Science Conference. Geochimica et Cosmochimica Acta Supplement* (1979), pp. 2031–2050.
29. L. Xie *et al.*, Crystallization of a hydrous magma ocean in the shallow lower mantle. *Earth Planet. Sci. Lett.* **633**, 118651 (2024).
30. T. Katsura *et al.*, Olivine-wadsleyite transition in the system (Mg, $Fe_)2Si_04$. *J. Geophys. Res. Solid Earth* **109**, B02209 (2004).
31. H. Fei, T. Katsura, Water solubility in fe-bearing wadsleyite at mantle transition zone temperatures. *Geophys. Res. Lett.* **48**, e2021GL092836 (2021).
32. A. C. Withers, M. M. Hirschmann, T. J. Tenner, The effect of Fe on olivine H_2O storage capacity: Consequences for H_2O in the Martian mantle. *Am. Mineral.* **96**, 1039–1053 (2011).
33. H. Fei, T. Katsura, Pressure dependence of proton incorporation and water solubility in olivine. *J. Geophys. Res. Solid Earth* **125**, e2019JB018813 (2020).
34. A. Gale, C. A. Dalton, C. H. Langmuir, Y. Su, J. Schilling, The mean composition of ocean ridge basalts. *Geochem., Geophys., Geosystems* **14**, 489–518 (2013).
35. S. Qian *et al.*, Highly heterogeneous mantle caused by recycling of oceanic lithosphere from the mantle transition zone. *Earth Planet. Sci. Lett.* **593**, 117679 (2022).
36. M. Li, "The cycling of subducted oceanic crust in the earth's deep mantle" in *Mantle Convection and Surface Expressions*, H. Marquardt, M. Ballmer, S. Cottaar, J. Konter, Eds. (2021), pp. 303–328.
37. J. Feng, H. Yao, Y. Wang, P. Poli, Z. Mao, Segregated oceanic crust trapped at the bottom mantle transition zone revealed from ambient noise interferometry. *Nat. Commun.* **12**, 2531 (2021).
38. A. E. Ringwood, Role of the transition zone and 660 km discontinuity in mantle dynamics. *Phys. Earth Planet. Inter.* **86**, 5–24 (1994).
39. C. Yu, S. Goes, E. A. Day, R. D. van der Hilst, Seismic evidence for global basalt accumulation in the mantle transition zone. *Sci. Adv.* **9** (2023).
40. B. Tauzin, L. Waszek, M. D. Ballmer, J. C. Afonso, T. Bodin, Basaltic reservoirs in the Earth's mantle transition zone. *Proc. Nat. Acad. Sci.* **119**, e2209399119 (2022).
41. D. Bondar, H. Fei, A. C. Withers, T. Katsura, A rapid-quench technique for multi-anvil high-pressure-temperature experiments. *Rev. Sci. Instrum.* **91**, 065105 (2020).
42. L. Stixrude, C. Lithgow-Bertelloni, Thermodynamics of mantle minerals–I. Physical properties. *Geophys. J. Int.* **162**, 610–632 (2005).
43. N. Miyajima, K. Fujino, N. Funamori, T. Kondo, T. Yagi, Garnet-perovskite transformation under conditions of the Earth's lower mantle: An analytical transmission electron microscopy study. *Phys. Earth Planet. Inter.* **116**, 117–131 (1999).
44. E. Van Cappellen, J. C. Doukhan, Quantitative transmission X-ray microanalysis of ionic compounds. *Ultramicroscopy* **53**, 343–349 (1994).
45. E. Van Cappellen, The parameterless correction method in X-ray microanalysis. *Microscopy Microanal. Microstruct.* **1**, 1–22 (1990).
46. L. Xie *et al.*, Low melt viscosity enables melt doublets above the 410-km discontinuity. *Nat. Commun.* **16**, 3239 (2025)
47. B. B. Karki, L. P. Stixrude, Viscosity of $MgSiO_3$ liquid at earth's mantle conditions: Implications for an early magma ocean. *Science* **1979**, 740–742 (2010).

Downloaded from https://www.pnas.org by WUHAN UNIVERSITY on June 23, 2025 from IP address 218.197.145.100.